ACS NANO

www.acsnano.org

W-Shaped Antiambipolar Transistors Based on h-BN/MoTe$_2$/BP Heterostructures

Enxiu Wu,* Yuexuan Ma, Qijia Tian, Zhiyuan Wang, Zhaoqi Song, Shida Huo, Fanying Meng, Yuan Xie, and Caofeng Pan

Cite This: *ACS Nano* 2025, 19, 35701−35711

Read Online

ACCESS | Metrics & More | Article Recommendations | Supporting Information

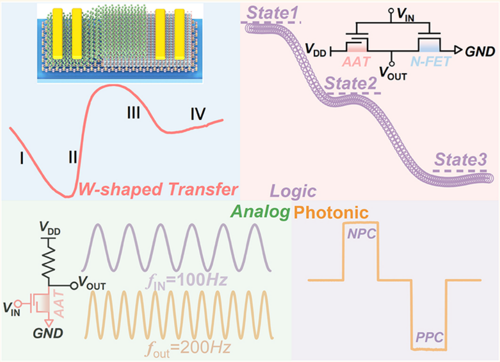

ABSTRACT: The development of multifunctional device architectures capable of integrating logic, analog, and optoelectronic functions is critical for overcoming the scaling and energy efficiency limitations of conventional CMOS technologies. Antiambipolar transistors (AATs), with their nonmonotonic transfer characteristics and central Λ-shaped region, provide an attractive platform for implementing multivalued logic operations, compact frequency multipliers, and photodetectors. Here, we present a high-performance W-shaped AAT based on an h-BN/MoTe$_2$/BP van der Waals heterostructure. The device exhibits four discrete conductance states and a symmetric Λ-region centered at V_{gs} = 0 V, with a high on/off current ratio exceeding 10^5 and peak currents in the microampere range. These properties enable the implementation of a ternary inverter with uniformly spaced 20 V logic windows and excellent operational stability over 200 switching cycles. In addition, the symmetric Λ-region facilitates bias-free frequency doubling, providing a low-power solution for analog signal processing. Furthermore, the device functions as a gate-tunable photovoltaic photodetector with dynamically reversible photocurrent polarity. It achieves a rectification ratio ranging from 10^{-3} to 10^3, a dark current below 0.5 pA, a photoresponsivity of 0.29 A/W, an external quantum efficiency (EQE) of 69.4%, and a fast response time of 100 μs. These results position W-shaped AATs as a potential platform for next-generation nanoelectronic and optoelectronic systems requiring reconfigurability, energy efficiency, and high integration density.

KEYWORDS: *antiambipolar transistor, multivalued logic, frequency doubling, van der Waals heterostructure, 2D materials*

INTRODUCTION

As traditional CMOS technology approaches its scaling and energy efficiency limits, the development of device architectures that can support higher integration density, lower power consumption, and greater functional complexity has become imperative for next-generation electronics.[1] Among emerging device concepts, The Antiambipolar Transistor (AAT)—a type field-effect transistor exhibits nonmonotonic transfer characteristic with prominent Λ-shaped region[2−5]—has attracted growing interest for its potential in multivalued logic operations,[6−9] signal processing,[10−14] and optoelectronic applications.[15−19] Unlike conventional frequency multipliers that require complex CMOS circuits, a single AAT can inherently perform frequency doubling,[10,13] significantly simplifying circuit design. Furthermore, ternary inverters based on AATs can reduce system complexity by up to 63.1%,[20,21] enhance information density, and streamline interconnect structures. The same device structure can simultaneously enable multivalued logic, frequency multiplication, and photodetection, highlighting the potential of functionally multiplexed architectures—an important trend for future semiconductor technologies.

The defining feature of an AAT lies in its sharp transconductance reversal, where positive and negative transconductance transitions occur within a narrow gate voltage range, this Λ-region can evolve into more complex profiles, such as N-,[7,22,23] И-,[9] or W-shaped transfer curves. Two-dimensional (2D) semiconductors offer a promising platform for realizing AATs due to their atomic thickness, excellent gate control, and strong light−matter interaction. Importantly, the 2D material family includes both p-type and n-type semiconductors, allowing the creation of van der Waals heterostructures without lattice-matching constraints. To

Received: July 14, 2025
Revised: September 25, 2025
Accepted: September 26, 2025
Published: October 3, 2025

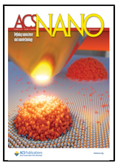

https://doi.org/10.1021/acsnano.5c11809

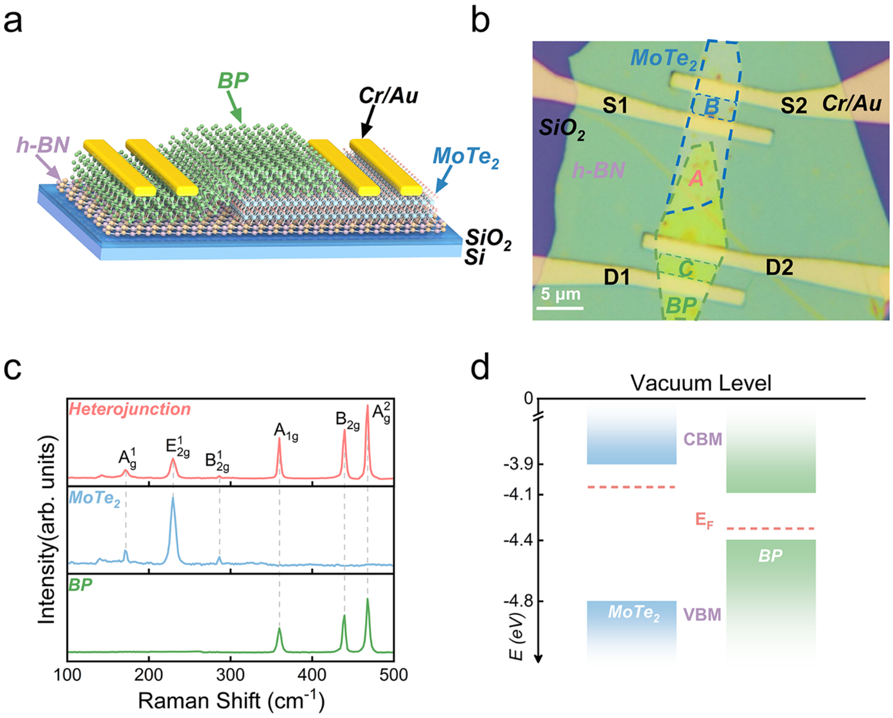

Figure 1. (a) Schematic illustration of the $MoTe_2$/BP heterojunction device fabricated on a Si/SiO_2/h-BN substrate. (b) Optical microscope image of the device, with D1, D2, S1, and S2 indicating the drain and source electrodes contacting $MoTe_2$ and BP, respectively. (c) Raman spectra of $MoTe_2$, BP, and the $MoTe_2$/BP junction region. (d) Energy band diagram of the $MoTe_2$/BP heterojunction, showing the electron affinities and bandgaps of the constituent materials.

date, a wide range of 2D heterostructures—such as WSe_2/MoS_2,[9,22,24] WSe_2/SnS_2,[22,25] WSe_2/InSe,[26] WSe_2/Graphene,[27] BP/MoS_2,[28,29] BP/ReS_2,[30,31] $MoTe_2$/MoS_2,[6,8,32] $MoTe_2$/InSe,[15] $MoTe_2$/Bi_2Se_3,[33] $MoTe_2$/CrOCl,[34] GeSe/SnS_2,[35] TaS_2/MoS_2[36]—have demonstrated antiambipolar behavior, supporting applications in ternary logic, frequency multiplication, gate-tunable rectification, and photodetection.

Despite this progress, several fundamental challenges remain. First, the realization of W-shaped AATs with four distinct conductance states is still rare and typically unstable, even within the same material system. Most reported devices exhibit N-shaped characteristics with only three conductance states, requiring precise alignment when constructing ternary logic gates. In contrast, W-shaped AATs inherently offer greater flexibility and fault tolerance, as any three of the four conductance states can be mapped to ternary logic levels and are, in principle, capable of enabling quaternary logic operation.[37] Second, the ability to precisely control the key parameters of the Λ-region—its position, width, and symmetry—remains limited. These characteristics critically impact logic level separation and frequency multiplication performance. A poorly controlled Λ-region can result in uneven logic windows or require large signal amplitudes for analog processing. A symmetric Λ-region centered around $V_{gs} = 0$ V enables bias-free frequency doubling, which is advantageous for reducing power consumption.[10,38] Third, while gate-tunable photodetection has been demonstrated in some AATs, dynamic and reversible photocurrent polarity switching has not yet been achieved.[15] This capability is essential for the development of intelligent, reconfigurable optoelectronic devices and would significantly expand the application space of AATs.

To address these challenges, we demonstrate a high-performance and multifunctional W-shaped AAT based on an h-BN/$MoTe_2$/BP van der Waals heterostructure. By tailoring the thickness of $MoTe_2$ and BP, we modulate the degree of bipolarity and shift the minimum conductance point, thereby enabling a symmetric Λ-region centered around $V_{gs} = 0$ V and achieving a stable W-shaped transfer characteristic. The device exhibits a peak current in the microampere range and an on/off ratio exceeding 10^5, outperforming most previously reported AATs. Leveraging these features, we construct a ternary inverter by connecting the AAT in series with an N-FET, achieving uniform 20 V logic windows across all states and maintaining less than 10% variation over 200 switching cycles. In addition, bias-free frequency doubling is realized due to the symmetric Λ-region, enabling low-power analog signal processing. Finally, benefiting from the favorable band alignment between $MoTe_2$ and BP, we develop a photovoltaic-type rectifying photodetector exhibiting gate-tunable and reversible rectification polarity and photocurrent direction. The device achieves a rectification ratio spanning 6 orders of magnitude (10^{-3}–10^3), a dark current below 0.5 pA, a photoresponsivity of 0.29 A/W, an external quantum efficiency (EQE) of 69.4%, and a response time of 100 μs, with less than 3% performance degradation after 1000 light on/off cycles. These results establish h-BN/$MoTe_2$/BP based W-shaped AATs as highly promising building blocks for multifunctional, reconfigurable, and energy-efficient nanoelectronic systems.

RESULTS AND DISCUSSION

The working principle of the AAT device based on a lateral heterojunction composed of h-BN, $MoTe_2$, and BP is illustrated in Figure 1a, where h-BN functions as a flat

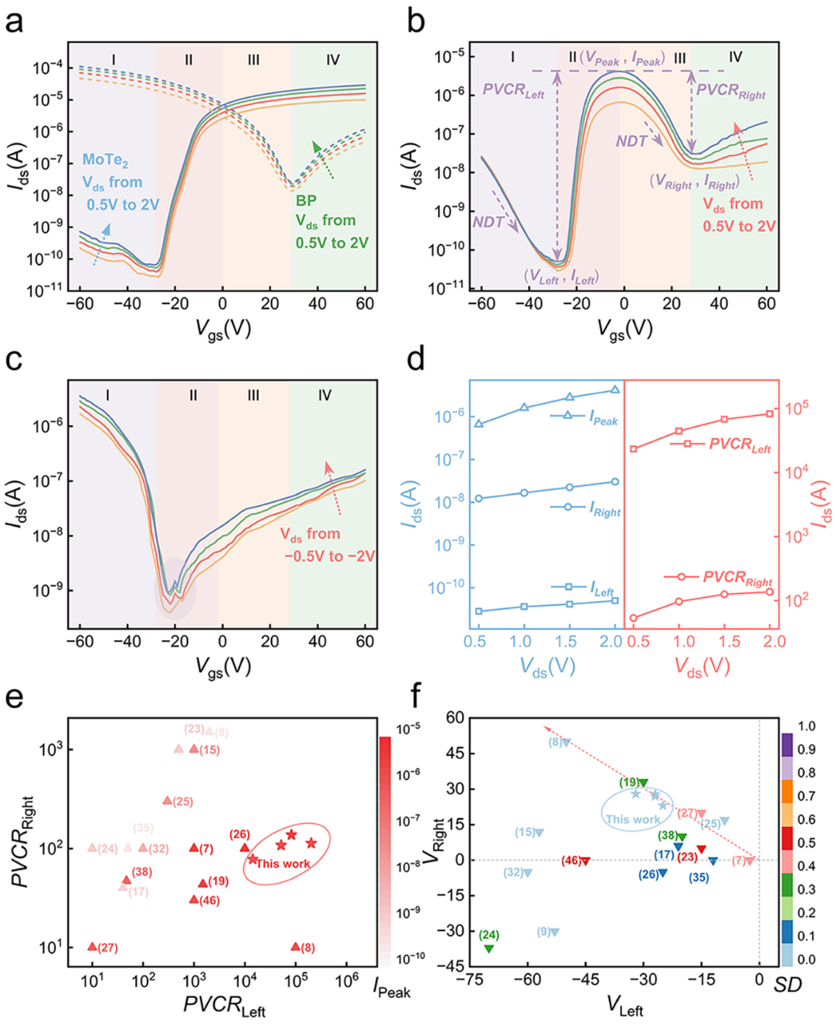

Figure 2. (a) Transfer characteristics of individual $MoTe_2$ (real lines) and BP (dash lines) transistors. (b,c) Transfer characteristics of the $MoTe_2$/BP heterojunction under forward (b) and reverse (c) drain−source voltage (V_{ds}) ranging from 0.5 to 2 V in steps of 0.5 V. (d) Peak current (I_{peak}), left/right valley currents (I_{Left}/I_{Right}), and peak-to-valley current ratios ($PVCR_{Left}/PVCR_{Right}$) of the heterojunction. (e) Comparison of the heterojunction's I_{Peak}, $PVCR_{Left}$, and $PVCR_{Right}$. (f) Comparison of the left and right cutoff voltages (V_{Left}/V_{Right}) and the symmetry degree (SD) of the heterojunction.

substrate to enhance device performance. Unlike the conventional SiO_2 substrate, which often exhibits surface roughness and a high density of trap states and impurities, h-BN effectively suppresses interfacial charge trapping and carrier scattering, thereby improving carrier mobility.[39−42] The detailed fabrication procedures are provided in the Experimental Section. Figure 1b shows the optical microscope image of the fabricated device, where $MoTe_2$ and BP are outlined by blue and green dashed lines, respectively. The yellow electrodes indicate that BP and $MoTe_2$ serve as the drain (D1, D2) and source (S1, S2), respectively, forming a lateral P−N junction. Atomic force microscopy (AFM) measurements, shown in Supplementary Figure S1, reveal that the thicknesses of h-BN, $MoTe_2$, and BP are approximately 28, 7.3, and 8.6 nm, respectively. Few-layer $MoTe_2$ and BP exhibit pronounced ambipolar characteristics and excellent gate tunability,[32,43] making them ideal candidates for AAT device fabrication. Figure 1c shows the Raman spectra of the device. For $MoTe_2$, characteristic peaks appear at 170 cm^{-1} (A_{1g}), 229 cm^{-1} (E^1_{2g}), and 286 cm^{-1} (B^1_{2g}), confirming that material adopts the hexagonal 2H phase. BP exhibits distinct Raman modes at 359 cm^{-1} (A_{1g}), 439 cm^{-1} (B_{2g}), and 467 cm^{-1} (A^2_g). These peaks are clearly observed in the $MoTe_2$/BP heterojunction region without any significant shifts, indicating good crystallinity, minimal strain, and the absence of phase transition at the interface. Figure 1d illustrates the energy band alignment of $MoTe_2$ and BP, with respective electron affinities of 3.9 and 4.1 eV, and bandgaps of 0.9 and 0.3 eV.[44,45]

Figure 2a presents the transfer characteristics of individual $MoTe_2$ (S1 as source and S2 as drain) and BP (D1 as source and D2 as drain) field-effect transistors (FET) measured under various drain-source voltages (V_{ds}) ranging from 0.5 to 2 V, with a gate-source voltage (V_{gs}) swept from −60 to 60 V. The $MoTe_2$ and BP FETs exhibit predominantly n-type and p-type ambipolar transport behaviors, respectively. The conductance minimum points are located at −28 V for $MoTe_2$ and 29 V for BP. The corresponding on/off ratios reach ∼10^5 (from ∼10^{-10} to 10^{-5}) for $MoTe_2$ and ∼10^4 (from ∼10^{-8} to 10^{-4}) for BP. Increasing V_{ds} enhances electric field across the channel, promoting carrier drift and resulting in elevated drain current and an overall upward shift of the transfer curves. As shown in Figure S2, the output characteristics of both $MoTe_2$ and BP exhibit nearly symmetric behavior under both forward and reverse V_{ds} without noticeable rectification, suggesting the

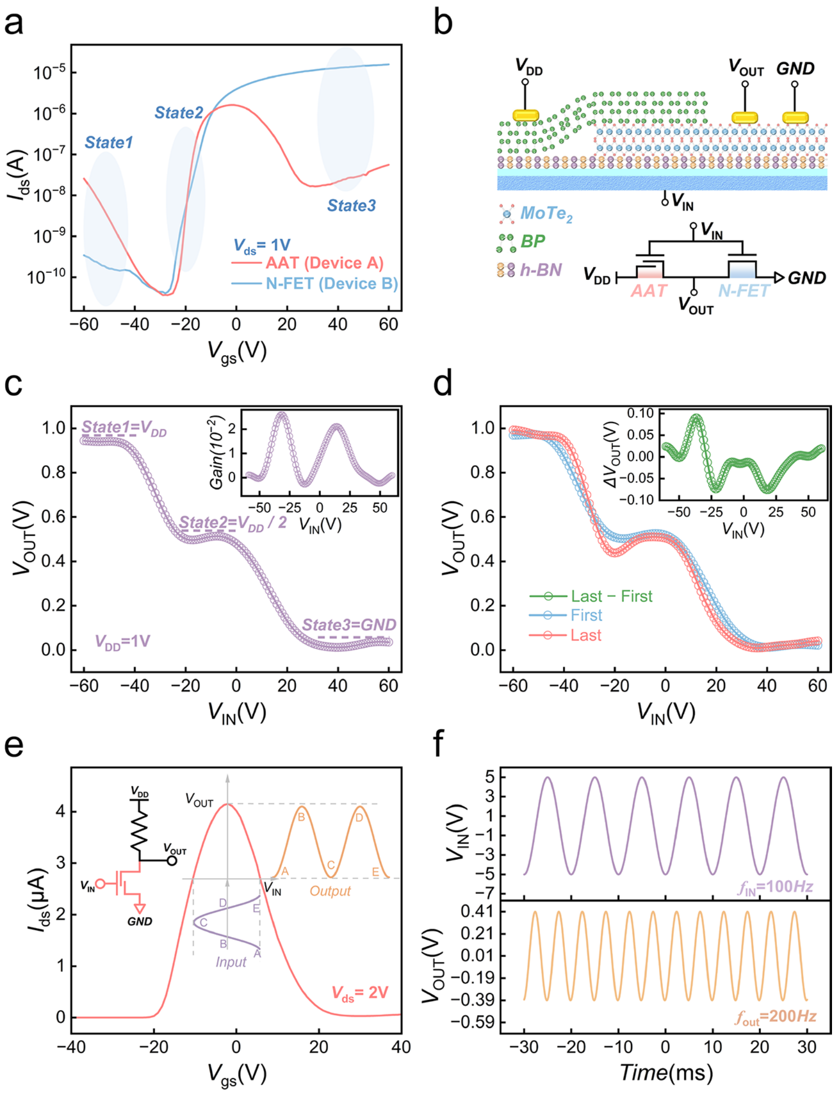

Figure 3. (a) Transfer characteristics of the AAT (red) and the N-FET (blue) at V_{ds} = 1 V. (b) Schematic diagram of the ternary inverter composed of an AAT (Device A) and an n-type FET (Device B) connected in series. (c) Voltage transfer curve and voltage gain (inset) of the ternary inverter at V_{DD} = 1 V. (d) Voltage transfer curves of the ternary inverter at V_{DD} = 1 V after 200 cycles, showing the first and last measurements; inset: difference between the two curves. (e) Schematic illustration of the frequency multiplier based on the Λ region of the AAT. (f) Measured input (purple) and output (yellow) waveforms of the frequency multiplier.

formation of near-ideal ohmic contacts with low contact resistance.

Figure 2b displays the transfer characteristics of the $MoTe_2$/BP heterojunction device (measured with S1 as source and D2 as drain) under forward bias ($V_{ds} > 0$), exhibiting a typical antiambipolar behavior. The curve presents a W-shaped profile, consisting of a pronounced central Λ-shaped conduction peak flanked by two low-conductance regions. Taking V_{ds} = 2 V as an example, the curve is divided into four distinct regions. In Region I (−60 to −27 V), both $MoTe_2$ and BP operate in the p-type conduction, and the heterojunction accordingly exhibits typical p-type transistor behavior with hole transport dominating. As the $MoTe_2$ becomes increasingly depleted, the drain current gradually decreases. At V_{gs} = −27 V, the current reaches a first local minimum (~5×10^{-11} A), defined as the left cutoff voltage (V_{Left}). In Region II (−27 to −1 V), $MoTe_2$ transitions from p-type to n-type conduction, leading to a rapid increase in drain current with positive differential transconductance. The peak current (~4×10^{-6} A) defines the Λ-region apex. In Region III (−1 to 28 V), the decreasing hole conduction in BP dominates over the increase electron conduction in $MoTe_2$, leading to negative differential transconductance and a second local minimum (~3×10^{-8} A) at V_{gs} = 28 V, defined as the right cutoff voltage (V_{Right}). In Region IV (28−60 V), BP transitions to n-type conduction resulting in a rise in drain current as both channels are conductive. As shown in Figure S3a, the transconductance undergoes a sharp polarity reversal at antiambipolar peak.

Under reverse bias ($V_{ds} < 0$), the transfer curve (Figure 2c) reveals enhanced current in Region I but suppressed conduction in Regions II and III, significantly weakening the antiambipolar behavior. The device instead exhibits a more conventional ambipolar response. This phenomenon can be attributed to the reversal of the built-in electric field direction within the heterojunction. Specifically, in Regions II and III, BP and $MoTe_2$ form a P−N junction with a built-in electric field directed from $MoTe_2$ to BP. Under reverse bias, the external electric field aligns with the built-in field, further suppressing carrier transport across the junction and reducing the current level, thereby weakening the antiambipolar effect. In contrast, in Region I, BP and $MoTe_2$ constitute a P^+-P^- junction, with the built-in field oriented from BP to $MoTe_2$. Under reverse bias, the external electric field opposes the built-in electric field, effectively reducing the total field strength and facilitating carrier transport, leading to an enhanced current in this region. This reversal of the built-in electric field direction not only accounts for the bias-dependent modulation of antiambipolar behavior, but also underlies the observed reversals in rectification ratio and photocurrent polarity, as further discussed in Figure 4.

Due to its W-shaped profile, the AAT exhibits three transconductance polarity inversion points. To quantify antiambipolar behavior, we define two peak-to-valley current ratios $PVCR_{Left}$ and $PVCR_{Right}$, as the ratio of the peak current (I_{peak}) to the left and right valley currents (I_{Left}, I_{Right}), respectively. Figure 2d shows the evolution of $I_{peak,}$ I_{Left}, I_{Right} and PVCR as functions of V_{ds}. Forward bias pulls down the BP energy band, reduces the energy barrier, and enhances the peak current, thereby improving PVCR.[7,46] At V_{ds} = 2 V, $PVCR_{Left}$ and $PVCR_{Right}$ reach 10^5 and 10^2, respectively—outperforming most previously reported AATs (Figure 2e). Although a few devices in literature show slightly higher $PVCR_{Right}$, their peak currents are significantly lower, which limits their actual load-driving capability. The combination of ultrahigh switching ratio and large peak current endows our device with excellent logic state distinguishability and driving performance.

To achieve low-power frequency doubling, the Λ-region should ideally be symmetric around V_{gs} = 0 V requiring $|V_{Left}| \approx |V_{Right}|$ and $V_{Peak} \approx 0$ V. Figure 2f compares the cutoff voltages in previously reported AATs, introducing a symmetry deviation (SD) coefficient defined as $SD = 2 \times |V_{Peak} - V_{center}|/(V_{right} - V_{Left})$, $V_{center} = (V_{right} + V_{Left})/2$. A smaller SD indicates greater Λ-region symmetry. Our device, located near the $|V_{Left}| = |V_{Right}|$ line in Figure 2f, achieves an SD of 0.055, outperforming most prior reports. This is further confirmed by the linear-scale transfer curve (Figure S3b). The symmetry arises from matched cutoff voltages and balanced transfer characteristics of $MoTe_2$ and BP around V_{gs} = 0 V (Figure S3c), facilitating full antiambipolar response at low gate bias.

The nonoverlapping channel lengths of $MoTe_2$ and BP also influence the current in Regions I, II, and Regions III, IV, respectively. As shown in Figure S3a,d shorter channel generally increases the current in its respective region of influence. Notably, a short-channel $MoTe_2$ effectively enhances the current in Region I and enables the heterojunction to exhibit a W-shaped profile, which is suitable for constructing a ternary inverter in series with an N-FET. Other samples also confirmed this phenomenon (Figure S4a,b). In contrast, prior work using strongly n-type MoS_2 and BP could only form N-shaped AAT, even with short channels—highlighting the advantage of employing ambipolar $MoTe_2$.[7,28,29]

In addition, when the BP electrode is directly fabricated on the overlapping heterojunction region (Figure S4c), the junction transitions from a lateral to a vertical configuration, and the antiambipolar behavior disappears (Figure S4d). This is because, in the vertical configuration, the thickness of BP becomes its effective channel length. Compared to lateral transport, where carriers must traverse longer in-plane distances, vertical transport spans only the material thickness, resulting in significantly reduced resistance.[47] Consequently, the overall transfer characteristic is dominated by the resistance of the laterally connected $MoTe_2$ segment.

As discussed above, the three transconductance polarity inversion points in the AAT transfer curve correspond to the conductance minimum points of $MoTe_2$ and BP, as well as the intersection of their transfer curves. In order to stably implement W-shaped AATs, we systematically measured the transfer characteristics of $MoTe_2$, BP, and heterojunctions with varying thicknesses (summarized in Figure S5i). When the thicknesses of both $MoTe_2$ and BP are confined to 8−15 nm (Figure S5a−c), both materials exhibit pronounced bipolar behavior with symmetric cutoff voltages producing a symmetric Λ-region and a W-shaped AAT.

For thicker flakes, gate control weakens, resulting in increased threshold voltages and weakened bipolar characteristics. If one material is significantly thicker than the other, the Λ-region in the AAT curve shifts markedly (Figure S5d,e) and the antiambipolar behavior severely deteriorates (Figure S5f,g). When both channels are excessively thick, complete depletion cannot be achieved, leading to the disappearance of antiambipolar characteristics (Figure S5h).

By comparing the transfer characteristics of the AAT and the N-FET (Figure 3a), three distinct regimes can be identified in which the conductance of the AAT is lower than, comparable to, or higher than that of the N-FET as the gate voltage varies. Leveraging this relationship, we propose a ternary inverter architecture comprising an AAT and an N-FET that reliably achieves stable three level logic output. Figure 3b illustrates the device configuration and operating principle. One terminal of the AAT is connected to the supply voltage (V_{DD}), while the other is linked to the N-FET, forming a shared output node (V_{OUT}). The remaining terminal of the N-FET is grounded (GND). The input voltage (V_{IN}) is applied simultaneously to the gates of both the AAT and the N-FET, controlling the logic state of the inverter.

The ternary logic output of this architecture originates from the conductance matching between the AAT and the N-FET across different V_{IN} regions. Figure 3c shows the voltage transfer characteristics of the ternary inverter. In the V_{IN} range from −20 to 0 V, both AAT and $MoTe_2$ exhibit comparable conductance, leading to nearly equal voltage division across them and an output voltage of $V_{OUT} \approx V_{DD}/2$, corresponding to State 2 (intermediate level) in Figure 3c. From −60 to −40 V, the AAT is in a low-resistance conducting state, while the N-FET remains in a high-resistance state. Consequently, most of the voltage falls on the N-FET, and the output is pulled up by the conducting AAT to a high voltage level ($V_{OUT} \approx V_{DD}$), corresponding to State 1. Conversely, in the range of 30−60 V, the AAT transitions into a high-resistance state, whereas the N-FET is turned on, pulling the output down to a low level ($V_{OUT} \approx 0$ V), corresponding to State 3. The inset of Figure 3c shows the voltage gain with two distinct peaks. The lower gain can be optimized by using a high-k dielectric substrate.[48] Figure S6a shows the voltage transfer curves and gains of the ternary inverter under various V_{DD}, all showing well-defined ternary logic levels. To evaluate the device stability, 200 consecutive switching cycles were performed, with results summarized in Figure S6b. Figure 3d compares the voltage transfer curves from the first and final cycles, and the inset highlights their difference to estimate error margins. All variations in output levels remain within 10%, with no noticeable level shift or degradation, confirming excellent operational stability during repeated state transitions.

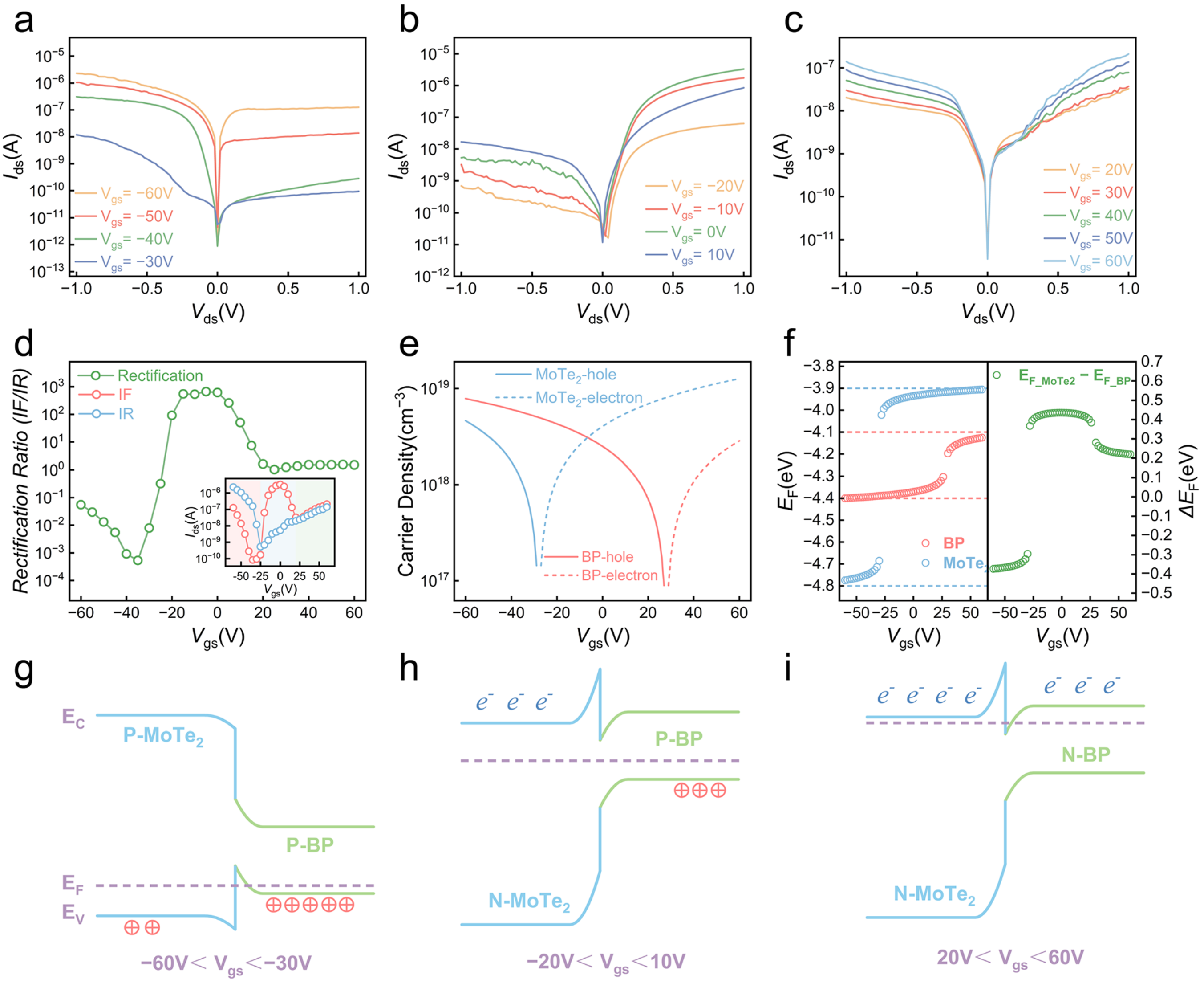

Figure 4. (a−c) Output characteristics of the heterojunction under different V_{gs} ranges: (a) −60 to −30 V, (b) −20 to 10 V, and (c) 20−60 V. (d) Rectification ratio (IF/IR) of the heterojunction as a function of V_{gs}. The inset shows the forward (V_{ds} = 1 V) and reverse (V_{ds} = −1 V) current as a function of V_{gs}. (e) Carrier density and carrier type of MoTe$_2$ (blue) and BP (red) as a function of V_{gs}. (f) Fermi level positions of MoTe$_2$ (blue) and BP (red) as a function of V_{gs}, with the green curve representing the difference in Fermi levels between the two materials. (g−i) Energy band diagrams of the MoTe$_2$/BP heterojunction under different V_{gs}, corresponding to (g) P$^+$−P$^-$ junction, (h) P−N junction, and (i) N−N junction.

Furthermore, the input voltage windows corresponding to the three logic states maintain a width of approximately 20 V, providing a broad tolerance margin that helps reduce error rates. To further verify the general applicability of this device architecture, a ternary inverter was fabricated on additional sample and tested. The results, shown in Figure S6c,d, display the transfer characteristics of AAT and N-FET and the corresponding ternary inverter voltage transfer curve, all demonstrating stable ternary logic responses, confirming the reproducibility of the design.

Owing to the symmetric transfer characteristics of the AAT in the Λ-region, the device exhibits excellent frequency multiplier capability without requiring additional bias voltages. Figure 3e illustrates the operating principle of the frequency multiplier based on the AAT. As shown in the inset, a sinusoidal input signal is applied to the gate (V_{IN}) via a signal generator, and the output signal (V_{OUT}) is monitored using an oscilloscope. During one-half-cycle of the input signal (from point A to point C), the output signal completes a full cycle, indicating a successful frequency doubling. Figure 3f presents the experimental results under V_{DD} = 2 V. When a 100 Hz sinusoidal signal with a 10 V peak-to-peak voltage is applied as the input, the output exhibits a doubled frequency of 200 Hz, confirming the device's ability to achieve low-power frequency multiplication without external bias and the potential of the AAT-based device for energy-efficient analog signal processing applications. By employing thinner SiO$_2$ layers or high-k dielectrics, the required input voltage window can be effectively reduced, further increasing switching speed and reducing dynamic power consumption.

In addition to the versatile functionalities enabled by the transfer characteristics, the output curves also exhibit pronounced rectifying behavior, with the rectification polarity reversibly tuned by V_{gs}. Specifically, when the V_{gs} is in the range of −60 to −30 V (Figure 4a), the reverse current (IR) is higher than the forward current (IF), indicating strong

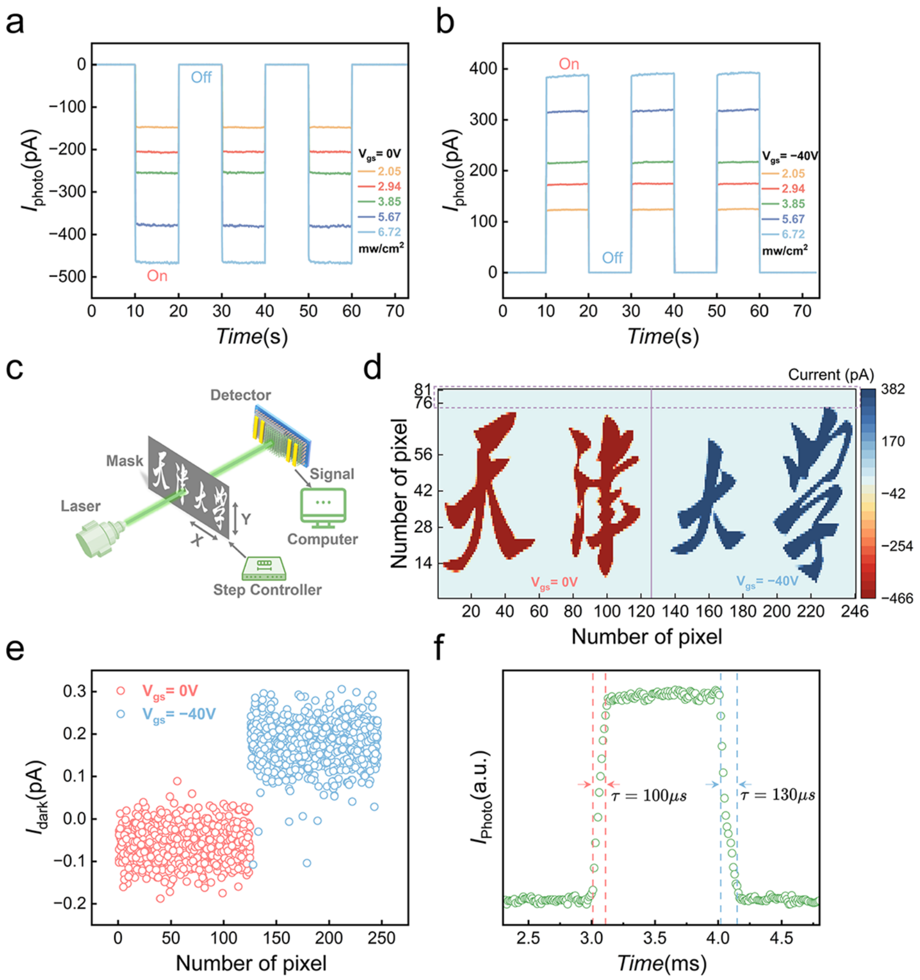

Figure 5. (a,b) Photocurrent response of the heterojunction under 520 nm laser illumination with varying incident power at (a) V_{gs} = 0 V and (b) −40 V. (c) Schematic diagram of the device photocurrent imaging system. (d) 81 × 246 pixels photocurrent image of the 'Tianjin University' pattern, where the characters 'Tianjin' are imaged at V_{gs} = 0 V and 'University' at −40 V under 520 nm laser illumination with an incident power of 6.72 mW/cm². (e) Extracted dark current values from rows 76 to 81 in (d). (f) Time-resolved photocurrent of the device under 520 nm laser illumination at V_{gs} = 0 V.

rectification. Between −20 and 10 V (Figure 4b), IF increases rapidly and exceeds IR, resulting in a reversal of the rectification direction. As the V_{gs} is further increased to the range of 20−60 V (Figure 4c), IF and IR gradually become comparable, and the rectification effect is significantly diminished.

To more intuitively illustrate this tunable rectification behavior, we extracted the IF and IR at V_{ds} = ±1 V from Figure 4a−c and plotted them along with rectification ratio (IF/IR) as a function of V_{gs} in Figure 4d. As V_{gs} increases from −60 to 20 V, the rectification ratio undergoes a polarity reversal. Notably, the ratio changes dramatically by 6 orders of magnitude (from 10^{-3} to 10^{3}) within a narrow V_{gs} window of −35 to −15 V, demonstrating exceptional gate-tunable rectification performance.

As previously analyzed, near-ohmic contacts are formed between electrodes and channel materials, indicating that the observed rectification behavior primarily originates from the built-in potential at the heterojunction interface. Ideally, this built-in potential is determined by the Fermi level difference between the two materials before contact. As the V_{gs} varies, the relative positions of the Fermi levels of the constituent materials shift accordingly, modulating both the direction and magnitude of the built-in potential. These changes ultimately influence the magnitude and polarity of the rectification ratio.

To intuitively explain the Fermi level shifts, we first establish the relationship between carrier density and V_{gs} using the following formula:

$$n_e/n_h = \frac{C_G|V_{gs} - V_{th}|}{qt}$$

Here, n_e and n_h represent the density of electrons and holes, respectively, q is the elementary charge, t is the thickness, and V_{th} is the threshold voltage. C_G denotes SiO_2 and h-BN series capacitance. The calculated results are shown in Figure 4e. Subsequently, the Fermi level positions of $MoTe_2$ and BP under different Vgs are calculated using the following equations:

$$E_F = \begin{cases} E_C + k_B T \ln \dfrac{n_e}{N_C} \\ E_V - k_B T \ln \dfrac{n_h}{N_V} \end{cases}$$

where E_C and E_V denote the conduction band minimum and valence band maximum, k_B is the Boltzmann constant, T is the temperature, N_c and N_v are the effective density of states in the conduction and valence bands, respectively. The detailed calculations for carrier density and Fermi level positions are provided in S7.

Figure 4f shows the Fermi levels of $MoTe_2$ and BP, along with their differences, as a function of V_{gs}. Near the conductance minimum points, even slight variations in V_{gs} can significantly shift the Fermi level of the materials, causing them to rapidly traverse the bandgap and approach either the conduction band minimum. This leads to pronounced variations in both the magnitude and sign of the Fermi level difference between $MoTe_2$ and BP. Notably, this phenomenon closely corresponds to the polarity reversal of the rectification ratio observed in two gate voltage regions (−30 to −20 V and 10−30 V) in Figure 4d, further confirming that the relative Fermi level alignment is the underlying mechanism driving the rectification polarity reversal.

In conjunction with the schematic energy band diagrams shown in Figure 4g−i, it is evident that when the V_{gs} ranges from −60 to −30 V, the Fermi levels of both $MoTe_2$ and BP lie near their respective valence band maximum, indicating p-type conduction in both materials. BP exhibits a higher hole concentration and stronger p-type behavior and the heterostructure forms a P^+−P^- junction, with a built-in electric field directed from BP to $MoTe_2$. As the V_{gs} increases to the range of −20 to 10 V, the Fermi level of $MoTe_2$ rapidly shifts toward the conduction band minimum, resulting in n-type conduction. This transition forms a P−N junction with the still p-type BP. Due to the relative shift in Fermi level, the built-in electric field reverses direction, now directed from $MoTe_2$ to BP. Under reverse V_{ds} bias, the external electric field aligns with the built-in field, enhancing the interfacial barrier and suppressing carrier transport across the junction. Consequently, IR decreases and becomes smaller than the IF, leading to a reversal in the rectification ratio. When the V_{gs} further increases above 20 V, the Fermi level of BP also approaches its conduction band minimum, and both $MoTe_2$ and BP exhibit n-type behavior, forming an N−N junction. With comparable carrier concentrations in both materials, no significant carrier density gradient exists at the interface, resulting in the disappearance of the built-in potential. As a result, the heterojunction no longer shows prominent rectification behavior.

From a functional perspective, the device can be regarded as a polarity-tunable 2D diode, with rectification primarily originating from the $MoTe_2$/BP heterojunction region. The rectification polarity can be effectively modulated by the V_{gs}. This device features a simple architecture, achieving rapid rectification polarity switching within a relatively narrow V_{gs} range using a single gate. This eliminates the need for complex fabrication processes and redundant control required by conventional dual-gate structures,[49] making it a promising candidate for high-density, low-power multifunctional electronic applications.

The direction of the built-in electric field also determines the drift direction of photogenerated carriers, enabling the device to exhibit a polarity-switchable photoresponse under different V_{gs}. Figure 5a,b show the photocurrent response of the device under 520 nm laser illumination with varying incident power at V_{gs} = 0 and −40 V, respectively. In both cases, the absolute value of the photocurrent increases with increasing incident power. At V_{gs} = 0 V, the heterostructure forms a P−N junction, with the built-in electric field pointing from $MoTe_2$ to BP. Photogenerated electrons and holes drift toward $MoTe_2$ and BP, respectively, resulting in a negative photocurrent (Figure 5a). In contrast, at V_{gs} = −40 V, the structure transitions to a P^+−P^- junction, with the built-in electric field pointing from BP to $MoTe_2$. In this case, electrons and holes drift toward BP and $MoTe_2$, respectively, yielding a positive photocurrent (Figure 5b).

Under an incident power of 6.72 mW/cm^2, the device achieves a maximum photoresponsivity of 0.29 A/W and an external quantum efficiency (EQE) of 69.4%. The output characteristics under different incident powers and gate voltages are shown in Figure S8. At V_{gs} = −40 V, the device exhibits a negative open-circuit voltage and a positive photocurrent (Figure S8a,c), while at V_{gs} = 0 V, a positive open-circuit voltage and negative photocurrent are observed (Figure S8b,d). Furthermore, Figure S9 illustrates the dependence of both rectification ratio and photocurrent on V_{gs}, revealing that their reversals occur nearly simultaneously. Combined with the analysis of the rectification mechanism, this observation further confirms that the variation in gate voltage alters the relative Fermi level positions of $MoTe_2$ and BP, thereby reversing the direction of the built-in electric field, which is the fundamental cause of the polarity switching in both rectification ratio and photocurrent.

To further demonstrate the potential of this device for practical applications, we designed imaging experiments based on its photoelectric response characteristics. Figure 5c illustrates the schematic of the photoelectric imaging system. The device was illuminated with a 520 nm laser at an incident power of 6.72 mW/cm^2 and a mask was moved between the laser source and the device to produce an 81 × 246-pixel image, as shown in Figure 5d. The left and right parts of the image were obtained under V_{gs} = 0 and −40 V, respectively. Four distinct characters, 'Tianjin University', can be clearly observed, indicating good consistency in photocurrent response under the same V_{gs}.

Figure 5e shows the extracted dark current values from rows 76 to 81 in Figure 5d, with values consistently below 0.5 pA, corresponding to a signal-to-noise ratio of up to 10^3. The time-resolved photoresponse of the device is shown in Figure 5f, with response and recovery times of approximately 100 and 130 μs, respectively. To evaluate the device stability, we performed cyclic illumination tests using the 520 nm laser at 6.72 mW/cm^2. As shown in Figure S10, the device exhibited less than 3% variation over 1000 cycles, demonstrating excellent operational stability of the photoresponse.

CONCLUSION

In summary, we have demonstrated a high-performance W-shaped antiambipolar transistor (AAT) based on an h-BN/$MoTe_2$/BP vdWs heterostructure, offering a multifunctional platform that simultaneously supports logic, analog, and optoelectronic operations. By tailoring the thickness of $MoTe_2$ and BP, we engineered a symmetric Λ-region centered at V_{gs} = 0 V, enabling a stable four-state transfer characteristic with a high on/off current ratio exceeding 10^5 and micro-ampere-level peak currents. Leveraging these properties, we successfully implemented a ternary inverter with uniformly spaced 20 V logic levels and robust operation across 200 switching cycles. The symmetric Λ-region further facilitated bias-free frequency doubling, providing a low-power solution for analog signal processing. In addition, we realized a photovoltaic-type rectifying photodetector with gate-tunable and reversible photocurrent polarity, exhibiting a rectification ratio spanning 6 orders of magnitude, sub-pA dark current, fast response, and high EQE. This work not only overcomes key limitations in conventional AATs—including poor stability, asymmetry, and lack of optoelectronic reconfigurability—but also establishes a viable approach for integrating multivalued logic, analog frequency conversion, and intelligent photodetection within a single device. The demonstrated architecture highlights the potential of W-shaped AATs in energy-efficient, reconfigurable, and densely integrated nanoelectronic systems, paving the way for future multifunctional electronics based on 2D material heterostructures.

METHODS

Device Fabrication. Bulk h-BN, $MoTe_2$, and BP crystals were purchased from HQ Graphene. The heterostructures were fabricated using a dry transfer method. First, h-BN flakes were mechanically exfoliated from the bulk crystal and transferred onto a 285 nm SiO_2/n + doped Si substrate. Subsequently, a $MoTe_2$ flake was transferred onto the h-BN layer, followed by the stacking of a BP flake on top of the $MoTe_2$, forming a van der Waals heterostructure. The entire operation process is completed in the glovebox. Electrodes were defined using electron beam lithography (EBL) with a positive electron-beam resist. After exposure and development, a 15/60 nm Cr/Au metal stack was deposited via electron-beam evaporation. The fabrication process was completed with a standard lift-off procedure.

Characterization and Test. We used a commercial Raman spectrometer (Renishaw, Inc.) to perform the Raman spectroscopy with a 532 nm laser source. The AFM images were taken with Bruker Dimension Icon. The electrical properties were measured with an Agilent B1500A semiconductor parameter analyzer in vacuum. The photoelectric performance of the device was tested using the Metatest E2 photoelectric testing system from Nanjing Metatest Optoelectronics Co., Ltd. The photovoltaic properties were performed with a laser 520 nm in wavelength, the power of which can be tuned continually. We used an optical power meter of PM100D to measure the power of the light and calculated the incident light power on the devices according to their area.

ASSOCIATED CONTENT

Supporting Information

The Supporting Information is available free of charge at https://pubs.acs.org/doi/10.1021/acsnano.5c11809.

> Thickness characterization using AFM; output characteristics of $MoTe_2$/BP heterojunction devices; measurements with varying channel lengths; vertical heterojunction device testing; antiambipolar behavior tests for devices with different thicknesses; ternary logic reproducibility tests; theoretical calculation of carrier concentration; photoilluminated output characteristics of the heterojunction; the relationship between rectification ratio and photocurrent; and photodetection reproducibility tests (PDF)

AUTHOR INFORMATION

Corresponding Author

Enxiu Wu − *State Key Laboratory of Precision Measurement Technology and Instruments, School of Precision Instruments and Optoelectronics Engineering, Tianjin University, Tianjin 300072, China; School of Electronics and Information Engineering, Tiangong University, Tianjin 300387, China;* orcid.org/0000-0001-6060-1180; Email: enxiuwu@tju.edu.cn

Authors

Yuexuan Ma − *State Key Laboratory of Precision Measurement Technology and Instruments, School of Precision Instruments and Optoelectronics Engineering, Tianjin University, Tianjin 300072, China*

Qijia Tian − *State Key Laboratory of Precision Measurement Technology and Instruments, School of Precision Instruments and Optoelectronics Engineering, Tianjin University, Tianjin 300072, China*

Zhiyuan Wang − *State Key Laboratory of Precision Measurement Technology and Instruments, School of Precision Instruments and Optoelectronics Engineering, Tianjin University, Tianjin 300072, China*

Zhaoqi Song − *State Key Laboratory of Precision Measurement Technology and Instruments, School of Precision Instruments and Optoelectronics Engineering, Tianjin University, Tianjin 300072, China*

Shida Huo − *State Key Laboratory of Precision Measurement Technology and Instruments, School of Precision Instruments and Optoelectronics Engineering, Tianjin University, Tianjin 300072, China*

Fanying Meng − *State Key Laboratory of Precision Measurement Technology and Instruments, School of Precision Instruments and Optoelectronics Engineering, Tianjin University, Tianjin 300072, China*

Yuan Xie − *State Key Laboratory of Precision Measurement Technology and Instruments, School of Precision Instruments and Optoelectronics Engineering, Tianjin University, Tianjin 300072, China; School of Electronics and Information Engineering, Tiangong University, Tianjin 300387, China*

Caofeng Pan − *Institute of Atomic Manufacturing, Beihang University, Beijing 100191, P. R. China;* orcid.org/0000-0001-6327-9692

Complete contact information is available at: https://pubs.acs.org/10.1021/acsnano.5c11809

Author Contributions

Y.M. carried out the experiments, analyzed the data, and wrote the manuscript. E.W. and Y.X. oversaw all phases of the research and revised the manuscript. Z.S. and Z.W. constructed device models and schematics and revised the manuscript. S.H. and Q.T. assisted in data processing and conducted supplementary measurements. F.M. contributed to literature review and assisted in device fabrication. C.P. provided conceptual guidance and supervised the project.

Notes

The authors declare no competing financial interest.

ACKNOWLEDGMENTS

This study was supported by the National Science Foundation of China [Grant Nos. 62304151, 62204170, and 62474124], the Natural Science Foundation of Tianjin [Grant No. 22JCQNJC01010], the open research of Songshan Lake Materials Laboratory [Grant No. 2023SLABFK07], the China Postdoctoral Science Foundation [No. 2023M742585], the State Key Laboratory of Fluid Power and Mechatronic Systems under Grant [No. GZKF-202327], the State Key Laboratory of Mechanics and Control for Aerospace Structures (Nanjing University of Aeronautics and astronautics) [Grant No. MCMS-E-0123Y01], and the Open Project of State Key Laboratory of Transducer Technology [Grant No. SKT2208].

REFERENCES

(1) Han, N.; Hou, J. J.; Wang, F.; Yip, S.; Yen, Y.-T.; Yang, Z.-x.; Dong, G.; Hung, T.; Chueh, Y.-L.; Ho, J. C. GaAs Nanowires: From Manipulation of Defect Formation to Controllable Electronic Transport Properties. *ACS Nano* **2013**, *7*, 9138−9146.

(2) Kim, J. H.; Moon, B. H.; Han, G. H. Anti-ambipolar transport and logic operation in two-dimensional field-effect transistors using in-series integration of GeAs and SnS2. *Appl. Phys. Lett.* **2024**, *124*, 123104.

(3) Cheng, R. Q.; Yin, L.; Wang, F.; Wang, Z. X.; Wang, J. J.; Wen, Y.; Huang, W. H.; Sendeku, M. G.; Feng, L. P.; Liu, Y. F.; et al. Anti-Ambipolar Transport with Large Electrical Modulation in 2D Heterostructured Devices. *Adv. Mater.* **2019**, *31*, No. 1901144.

(4) Wang, G. D.; Li, D.; Wang, X. Y.; Zhang, Y.; Zhang, H.; Wang, J. Antiambipolar, ambipolar, and unipolar charge transport in organic transistors based on a single vertical P-N heterointerface. *Journal of Materials Chemistry C* **2023**, *11*, 7283−7288.

(5) Lee, Y.; Kim, S.; Lee, H. I.; Kim, S. M.; Kim, S. Y.; Kim, K.; Kwon, H.; Lee, H. W.; Hwang, H. J.; Kang, S.; et al. Demonstration of Anti-ambipolar Switch and Its Applications for Extremely Low Power Ternary Logic Circuits. *ACS Nano* **2022**, *16*, 10994.

(6) Hu, R. X.; Wu, E. X.; Xie, Y.; Liu, J. Multifunctional anti-ambipolar p−n junction based on MoTe2/MoS2 heterostructure. *Appl. Phys. Lett.* **2019**, *115*, No. 073104.

(7) Huang, M. Q.; Li, S. M.; Zhang, Z. F.; Xiong, X.; Li, X. F.; Wu, Y. Q. Multifunctional high-performance van der Waals heterostructures. *Nat. Nanotechnol.* **2017**, *12*, 1148−1154.

(8) Wu, E. X.; Xie, Y.; Liu, Q. Z.; Hu, X. D.; Liu, J.; Zhang, D. H.; Zhou, C. W. Photoinduced Doping To Enable Tunable and High-Performance Anti-Ambipolar MoTe2/MoS2 Heterotransistors. *ACS Nano* **2019**, *13*, 5430−5438.

(9) Nourbakhsh, A.; Zubair, A.; Dresselhaus, M. S.; Palacios, T. Transport Properties of a MoS2/WSe2 Heterojunction Transistor and Its Potential for Application. *Nano Lett.* **2016**, *16*, 1359−1366.

(10) Yao, H.; Wu, E. X.; Liu, J. Frequency doubler based on a single MoTe2/MOS2 anti-ambipolar heterostructure. *Appl. Phys. Lett.* **2020**, *117*, 123103.

(11) Lee, M. J.; Kim, T. W.; Park, C. Y.; Lee, K. M.; Taniguchi, T.; Watanabe, K.; Kim, M. G.; Hwang, D.; Lee, Y. T. Graphene Bridge Heterostructure Devices for Negative Differential Transconductance Circuit Applications. *Nano-Micro Lett.* **2023**, *15*, 22.

(12) Jariwala, D.; Sangwan, V. K.; Seo, J. W. T.; Xu, W. C.; Smith, J.; Kim, C. H.; Lauhon, L. J.; Marks, T. J.; Hersam, M. C. Large-Area, Low-Voltage, Antiambipolar Heterojunctions from Solution-Processed Semiconductors. *Nano Lett.* **2015**, *15*, 416−421.

(13) Thakar, K.; Lodha, S. Multi-Bit Analog Transmission Enabled by Electrostatically Reconfigurable Ambipolar and Anti-Ambipolar Transport. *ACS Nano* **2021**, *15*, 19692.

(14) Zhu, Z. Y. S.; Persson, A. E. O.; Wernersson, L. E. Reconfigurable signal modulation in a ferroelectric tunnel field-effect transistor. *Nat. Commun.* **2023**, *14*, 2530.

(15) Sun, Y. M.; Gao, W.; Li, X. P.; Xia, C. X.; Chen, H. Y.; Zhang, L.; Luo, D. X.; Fan, W. J.; Huo, N. J.; Li, J. B. Anti-ambipolar behavior and photovoltaic effect in p-MoTe2/n-InSe heterojunctions. *Journal of Materials Chemistry C* **2021**, *9*, 10372−10380.

(16) Wang, Y.; Zhou, W. X.; Huang, L.; Xia, C. X.; Tang, L. M.; Deng, H. X.; Li, Y. T.; Chen, K. Q.; Li, J. B.; Wei, Z. M. Light induced double 'on' state anti-ambipolar behavior and self-driven photoswitching in p-WSe2/n-SnS2 heterostructures. *2D Mater.* **2017**, *4*, No. 025097.

(17) Wang, H. Y.; Gao, W.; Wen, P. T.; Yu, H.; Huang, Y.; Yue, Q.; Wang, X. Z.; Huo, N. J. Light-Regulated Anti-Ambipolar Transport with Multi-Logic States in Metal-WSe2-Metal Transistor. *Adv. Electron. Mater.* **2022**, *8*, No. 2200649.

(18) Huang, S.; Chen, H. Y.; Wang, S. J.; Chen, Y.; He, J. F.; Wang, W. H.; Pan, Y.; Zhao, Y. P.; Qi, L. G.; Su, S. C. Reversible charge-polarity control for a photo-triggered anti-ambipolar In2Se3&WSe2 heterotransistor. *Nanoscale* **2023**, *15*, 10223−10231.

(19) Zubair, M.; Xu, Y.; Wang, Y. Y.; Jiang, X. Y.; Miao, J. S.; Hao, S. L.; Tian, B. B.; Chu, J. H.; Duan, C. G. Van der Waals heterojunctions with negative differential transconductance for broadband photodetection, multi-valued logic, and artificial neuron. *InfoMat* **2025**, No. e70028.

(20) Jo, S. B.; Kang, J.; Cho, J. H. Recent Advances on Multivalued Logic Gates: A Materials Perspective. *Adv. Sci.* **2021**, *8*, No. 2004216.

(21) Jeong, J. W.; Choi, Y. E.; Kim, W. S.; Park, J. H.; Kim, S.; Shin, S.; Lee, K.; Chang, J.; Kim, S. J.; Kim, K. R. Tunnelling-based ternary metal-oxide-semiconductor technology. Nature. *Electronics* **2019**, *2*, 307−312.

(22) Li, Y. T.; Wang, Y.; Huang, L.; Wang, X. T.; Li, X. Y.; Deng, H. X.; Wei, Z. M.; Li, J. B. Anti-Ambipolar Field-Effect Transistors Based On Few-Layer 2D Transition Metal Dichalcogenides. *ACS Appl. Mater. Interfaces* **2016**, *8*, 15574−15581.

(23) Wu, D.; Li, W.; Rai, A.; Wu, X. Y.; Movva, H. C. P.; Yogeesh, M. N.; Chu, Z. D.; Banerjee, S. K.; Akinwande, D.; Lai, K. J. Visualization of Local Conductance in MoS2/WSe2 Heterostructure Transistors. *Nano Lett.* **2019**, *19*, 1976−1981.

(24) Kim, J. Y.; Park, H. J.; Lee, S. H.; Seo, C.; Kim, J.; Joo, J. Distinctive Field-Effect Transistors and Ternary Inverters Using Cross-Type WSe2/MoS2 Heterojunctions Treated with Polymer Acid. *ACS Appl. Mater. Interfaces* **2020**, *12*, 36530−36539.

(25) Lv, Y. H.; Wu, C. Y.; Zhao, Y.; Wu, G.; Abid, M.; Cho, J.; Choi, M.; Coileáin, C. O.; Hung, K. M.; Chang, C. R.; et al. Robust Anti-Ambipolar Behavior and Gate-Tunable Rectifying Effect in van der Waals p-n Junctions. *Acs Appl. Electron. Mater.* **2022**, *4*, 5487−5497.

(26) Inbaraj, C. R. P.; Mathew, R. J.; Ulaganathan, R. K.; Sankar, R.; Kataria, M.; Lin, H. Y.; Chen, Y. T.; Hofmann, M.; Lee, C. H.; Chen, Y. F. A Bi-Anti-Ambipolar Field Effect Transistor. *ACS Nano* **2021**, *15*, 8686−8693.

(27) Shim, J.; Jo, S. H.; Kim, M.; Song, Y. J.; Kim, J.; Park, J. H. Light-Triggered Ternary Device and Inverter Based on Heterojunction of van der Waals Materials. *ACS Nano* **2017**, *11*, 6319−6327.

(28) Wu, F.; Tian, H.; Yan, Z. Y.; Ren, J.; Hirtz, T.; Gou, G. Y.; Shen, Y.; Yang, Y.; Ren, T. L. Gate-Tunable Negative Differential Resistance Behaviors in a hBN-Encapsulated BP-MoS2 Heterojunction. *ACS Appl. Mater. Interfaces* **2021**, *13*, 26161−26169.

(29) Sangwan, V. K.; Beck, M. E.; Henning, A.; Luo, J. J.; Bergeron, H.; Kang, J. M.; Balla, I.; Inbar, H.; Lauhon, L. J.; Hersam, M. C. Self-Aligned van der Waals Heterojunction Diodes and Transistors. *Nano Lett.* **2018**, *18*, 1421−1427.

(30) Srivastava, P. K.; Hassan, Y.; Gebredingle, Y.; Jung, J.; Kang, B.; Yoo, W. J.; Singh, B.; Lee, C. Multifunctional van der Waals Broken-Gap Heterojunction. *Small* **2019**, *15*, No. 1804885.

(31) Xiong, X.; Kang, J. Y.; Hu, Q. L.; Gu, C. R.; Gao, T. T.; Li, X. F.; Wu, Y. Q. Reconfigurable Logic-in-Memory and Multilingual Artificial Synapses Based on 2D Heterostructures. *Adv. Funct. Mater.* **2020**, *30*, No. 1909645.

(32) Duong, N. T.; Lee, J.; Bang, S.; Park, C.; Lim, S. C.; Jeong, M. S. Modulating the Functions of MoS2/MoTe2 van der Waals Heterostructure via Thickness Variation. *ACS Nano* **2019**, *13*, 4478−4485.

(33) Tao, L.; Yao, B.; Yue, Q.; Dan, Z. Y.; Wen, P. T.; Yang, M. M.; Zheng, Z. Q.; Luo, D. X.; Fan, W. J.; Wang, X. Z.; et al. Vertically stacked Bi2Se3/MoTe2 heterostructure with large band offsets for nanoelectronics. *Nanoscale* **2021**, *13*, 15403−15414.

(34) Li, S. N.; Zhang, J. L.; Li, Y.; Zhang, K.; Zhu, L. Y.; Gao, W.; Li, J. B.; Huo, N. J. Anti-ambipolar and polarization-resolved behavior in MoTe2 channel sensitized with low-symmetric CrOCl. *Appl. Phys. Lett.* **2023**, *122*, No. 083503.

(35) Wu, L. W.; Gao, W.; Sun, Y. M.; Yang, M. M.; Zheng, Z. Q.; Fan, W. J.; Shu, K. X.; Dan, Z. Y.; Zhang, N.; Huo, N. J.; et al. Polarity-Switchable and Self-Driven Photo-Response Based on Vertically Stacked Type-III GeSe/SnS2 Heterojunction. *Adv. Mater. Interfaces* **2022**, *9*, No. 2102099.

(36) Mahajan, M.; Majumdar, K. Gate- and Light-Tunable Negative Differential Resistance with High Peak Current Density in 1T-TaS2/2H-MoS2 T-Junction. *ACS Nano* **2020**, *14*, 6803−6811.

https://doi.org/10.1021/acsnano.5c11809

(37) Andreev, M.; Choi, J. W.; Koo, J.; Kim, H.; Jung, S.; Kim, K. H.; Park, J. H. Negative differential transconductance device with a stepped gate dielectric for multi-valued logic circuits. *Nanoscale Horizons* **2020**, *5*, 1378−1385.

(38) Liu, Y.; Guo, J.; He, Q. Y.; Wu, H.; Cheng, H. C.; Ding, M. N.; Shakir, I.; Gambin, V.; Huang, Y.; Duan, X. F. Vertical Charge Transport and Negative Transconductance in Multilayer Molybdenum Disulfides. *Nano Lett.* **2017**, *17*, 5495−5501.

(39) Ahmed, F.; Kim, Y. D.; Choi, M. S.; Liu, X.; Qu, D. S.; Yang, Z.; Hu, J. Y.; Herman, I. P.; Hone, J.; Yoo, W. J. High Electric Field Carrier Transport and Power Dissipation in Multilayer Black Phosphorus Field Effect Transistor with Dielectric Engineering. *Adv. Funct. Mater.* **2017**, *27*, No. 1604025.

(40) Mahvash, F.; Paradis, E.; Drouin, D.; Szkopek, T.; Siaj, M. Space-Charge Limited Transport in Large-Area Monolayer Hexagonal Boron Nitride. *Nano Lett.* **2015**, *15*, 2263−2268.

(41) Ji, H.; Joo, M. K.; Yun, Y.; Park, J. H.; Lee, G.; Moon, B. H.; Yi, H.; Suh, D.; Lim, S. C. Suppression of Interfacial Current Fluctuation in MoTe2 Transistors with Different Dielectrics. *ACS Appl. Mater. Interfaces* **2016**, *8*, 19092−19099.

(42) Esqueda, I. S.; Tian, H.; Yan, X. D.; Wang, H. Transport Properties and Device Prospects of Ultrathin Black Phosphorus on Hexagonal Boron Nitride. *Ieee Transactions on Electron Devices* **2017**, *64*, 5163−5171.

(43) Yeom, D.; Ko, Y.; Ko, Y.; Im, H.; Song, J.; Seok, Y.; Jang, H.; Hwang, J.; Jin, S.; Watanabe, K.; et al. Ternary Transistors With Reconfigurable Polarities. *Adv. Funct. Mater.* **2025**, *35*, No. 2502112.

(44) Kang, J.; Tongay, S.; Zhou, J.; Li, J. B.; Wu, J. Q. Band offsets and heterostructures of two-dimensional semiconductors. *Appl. Phys. Lett.* **2013**, *102*, No. 012111.

(45) Cai, Y. Q.; Zhang, G.; Zhang, Y. W. Layer-dependent Band Alignment and Work Function of Few-Layer Phosphorene. *Sci. Rep.* **2014**, *4*, 6677.

(46) Zubair, M.; Wang, H. L.; Zhao, Q. X.; Kang, M. Y.; Xia, M. J.; Luo, M.; Dong, Y.; Duan, S. K.; Dai, F. X.; Wei, W. R.; et al. Gate-Tunable van der Waals Photodiodes with an Ultrahigh Peak-to-Valley Current Ratio. *Small* **2023**, *19*, No. 2300010.

(47) Gao, A. Y.; Zhang, Z. Y.; Li, L. F.; Zheng, B. J.; Wang, C. Y.; Wang, Y. J.; Cao, T. J.; Wang, Y.; Liang, S. J.; Miao, F.; et al. Robust Impact-Ionization Field-Effect Transistor Based on Nanoscale Vertical Graphene/Black Phosphorus/Indium Selenide Heterostructures. *ACS Nano* **2020**, *14*, 434−441.

(48) Yin, L.; Cheng, R.; Wan, X.; Ding, J.; Jia, J.; Wen, Y.; Liu, X.; Guo, Y.; He, J. High-κ monocrystalline dielectrics for low-power two-dimensional electronics. *Nat. Mater.* **2025**, *24*, 197.

(49) Shingaya, Y.; Zulkefli, A.; Iwasaki, T.; Hayakawa, R.; Nakaharai, S.; Watanabe, K.; Taniguchi, T.; Wakayama, Y. Dual-Gate Anti-Ambipolar Transistor with Van der Waals ReS2/WSe2 Heterojunction for Reconfigurable Logic Operations. *Adv. Electron. Mater.* **2023**, *9*, No. 2200704.